ChemComm

Chemical Communications

rsc.li/chemcomm

ROYAL SOCIETY
OF **CHEMISTRY**
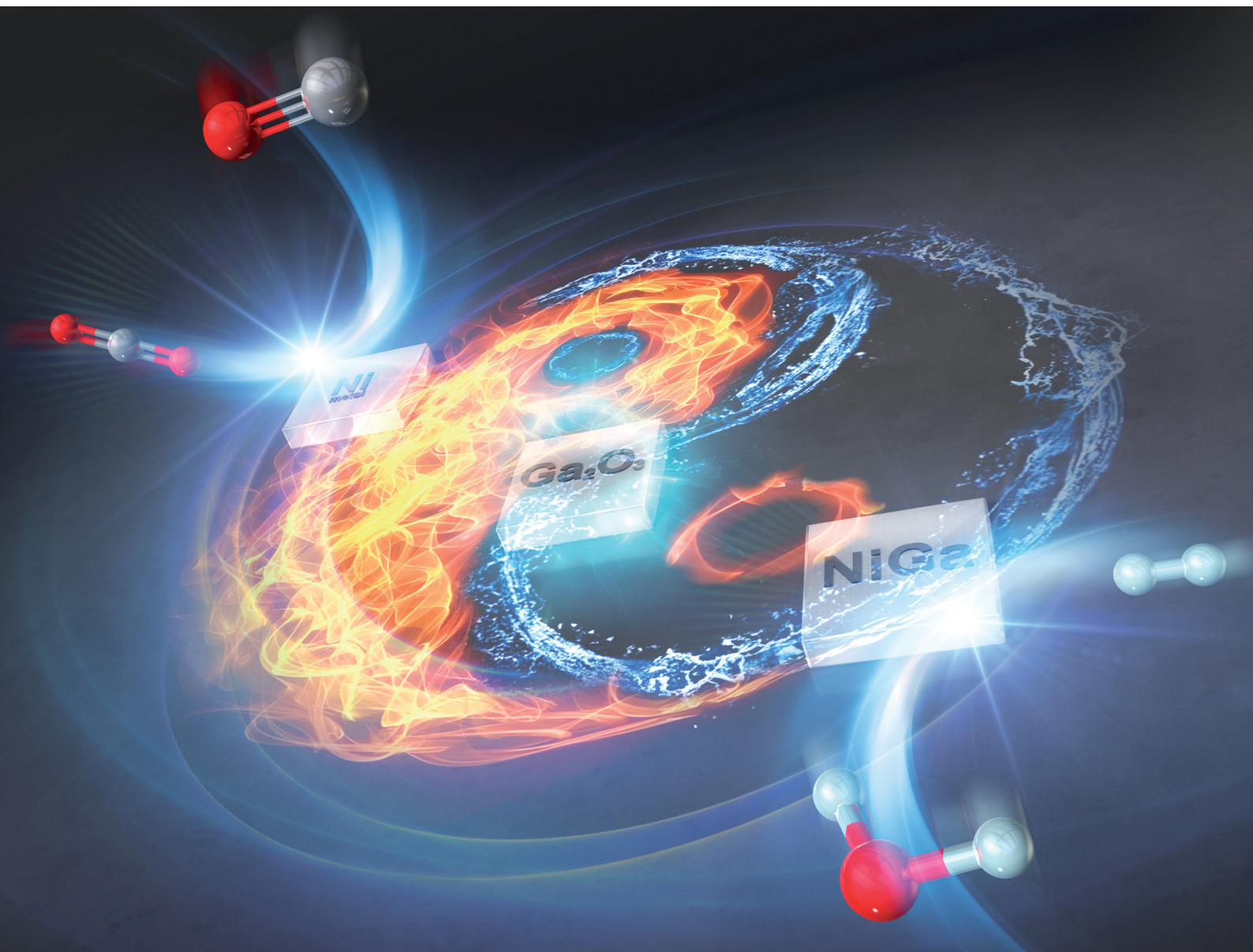
COMMUNICATION
Yasushi Sekine *et al.*
Equilibrium unconstrained low-temperature CO$_2$ conversion
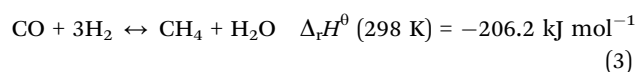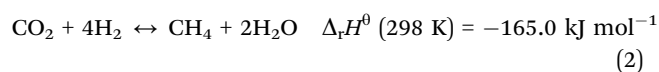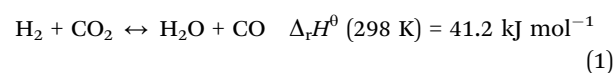on doped gallium oxides by chemical looping

Check for updates

Equilibrium unconstrained low-temperature CO_2 conversion on doped gallium oxides by chemical looping†

Keke Kang, Sota Kakihara, Takuma Higo, [ID] Hiroshi Sampei, [ID] Koki Saegusa and Yasushi Sekine [ID] *
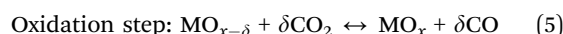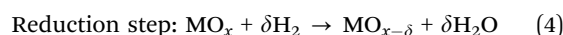
Reverse water gas shift (RWGS) can convert CO_2 into CO by using renewable hydrogen. However, this important reaction is endothermic and equilibrium constrained, and thus traditionally performed at 900 K or higher temperatures using solid catalysts. In this work, we found that RWGS can be carried out at low temperatures without equilibrium constraints using a redox method called chemical looping (CL), which uses the reduction and oxidation of solid oxide surfaces. When using our developed MGa_2O_x (M = Ni, Cu, Co) materials, the reaction can proceed with almost 100% CO_2 conversion even at temperatures as low as 673 K. This allows RWGS to proceed without equilibrium constraints at low temperatures and greatly decreases the cost for the separation of unreacted CO_2 and produced CO. Our novel gallium-based material is the first material that can achieve high conversion rates at low temperatures in reverse water gas shift using chemical looping (RWGS-CL). Ni outperformed Cu and Co as a dopant, and the redox mechanism of $NiGa_2O_x$ is a phase change due to the redox of Ga during the RWGS-CL process. This major finding is a big step forward for the effective utilization of CO_2 in the future.

As a greenhouse gas, carbon dioxide (CO_2) is emitted excessively from fossil fuel combustion, causing severe environmental difficulties.[1,2] Therefore, to achieve carbon neutrality, developing CO_2 capture and utilization (CCU) technologies that can accommodate sustainable recycling[3–6] is pivotally important. The reverse water gas shift (RWGS) reaction (eqn (1)) is a promising catalytic method to achieve "CO_2-to-CO" conversion using renewable H_2 as a reductant. The produced CO can be used flexibly for both methanol (MeOH) synthesis and downstream Fischer–Tropsch (F–T) processes to produce various liquid chemicals and fuels.[7,8] However, conventional RWGS is an endothermic and reversible reaction associated with

Department of Applied Chemistry, Waseda University, 3-4-1, Okubo, Shinjuku, Tokyo, 169-8555, Japan. E-mail: ysekine@waseda.jp

† Electronic supplementary information (ESI) available. See DOI: https://doi.org/10.1039/d3cc02399k

shortcomings such as high operating temperature, equilibrium constraints, unwanted side reactions of methanation (eqn (2) and (3)) and complicated separation of gaseous products.[3]

$$H_2 + CO_2 \leftrightarrow H_2O + CO \quad \Delta_r H^\theta \text{ (298 K)} = 41.2 \text{ kJ mol}^{-1} \tag{1}$$

$$CO_2 + 4H_2 \leftrightarrow CH_4 + 2H_2O \quad \Delta_r H^\theta \text{ (298 K)} = -165.0 \text{ kJ mol}^{-1} \tag{2}$$

$$CO + 3H_2 \leftrightarrow CH_4 + H_2O \quad \Delta_r H^\theta \text{ (298 K)} = -206.2 \text{ kJ mol}^{-1} \tag{3}$$

Conducting RWGS *via* chemical looping (RWGS-CL) can resolve the shortcomings of conventional processes because it can be separated into two sub-reactions (eqn (4) and (5)) using oxygen storage materials (OSMs). Consequently, the reduction (eqn (4)) and oxidation (eqn (5)) reactions can proceed at separate steps and sites.

$$\text{Reduction step: } MO_x + \delta H_2 \rightarrow MO_{x-\delta} + \delta H_2O \tag{4}$$

$$\text{Oxidation step: } MO_{x-\delta} + \delta CO_2 \leftrightarrow MO_x + \delta CO \tag{5}$$

In this way, the OSMs can be prevented from making contact with the products, thereby eliminating side reactions and simplifying gas separation. Reportedly, by evaluation of the solar-to-syngas energy efficiency, RWGS-CL can save 77% of the energy used for gas separation compared to conventional RWGS.[9] Moreover, RWGS-CL makes it possible to break the equilibrium barrier by the application of appropriate OSMs, thereby further improving energy efficiency and conserving energy. More importantly, the overall route for producing chemicals and fuels with RWGS-CL (Fig. S1, ESI†) can be carbon-neutral and sustainable if solar, electrical, or other non-fossil energy is used for hydrogen generation (*e.g.*, water splitting).[10]

The redox performance of OSMs is crucially important for RWGS-CL. Recently, much progress has been made to develop OSMs with excellent RWGS-CL performance, such as perovskite-structured oxides,[8,11–18] spinel-structured oxides,[19–21] Fe-based

oxides,[19–22] and In-based oxides.[23,24] Although experimental conditions such as H_2 or CO_2 feed gas concentrations and detection methods are not all the same in those studies, a recent report described that Co–In oxide showed the best CO_2 splitting rate of 0.28 mmol min^{-1} g^{-1} and a redox amount of 3.25 mmol g^{-1} at 773 K in comparison to other reported materials.[24] However, in practice, the low CO_2 equilibrium conversion of the oxidation step leads to a low concentration of the produced CO (the ratio of (CO/CO + CO_2)), increasing the cost of separating CO from CO_2 in the overall route with RWGS-CL (highlighted red box in Fig. S1, ESI†). Therefore, it is necessary to find proper OSMs that can make the oxidation step proceed forward rapidly even with a high CO concentration. Nevertheless, no study reported to date has particularly addressed this matter. Reportedly, the CO_2 oxidation step can proceed forward on Co–In$_2$O$_3$ with a 70–80% concentration of CO in the medium temperature region, but CO was not introduced simultaneously when evaluating the RWGS-CL performance.[24]

In this work, novel MGa$_2$O$_4$ (M = Ni, Cu, Co) spinel structured oxides were developed as OSMs with almost 100% CO_2 conversion even at lower temperature and Ni outperforms Cu and Co as a dopant in the redox amount and CO_2 splitting rate. The method for measuring the maximum CO_2 conversion of the oxidation step, the procedure for the RWGS-CL cycling test and the related definitions for evaluating the performance are also described in the ESI† text.

To elucidate the reaction mechanisms of the NiGa$_2$O$_x$ material, powder X-ray diffraction (XRD), transmission electron microscopy with energy-dispersive X-ray spectroscopy (STEM-EDX), Brunauer–Emmett–Teller (BET) measurement and *in situ* X-ray absorption fine structure (*in situ* XAFS) were conducted to characterize the structural features. Moreover, the redox behaviors of the MGa$_2$O$_x$ (M = Ni, Cu, Co) oxides were characterized by H_2 temperature-programmed reduction (H_2-TPR) and CO_2 temperature-programmed oxidation (CO_2-TPO). Kinetics analysis was also conducted to elucidate the oxidation behavior of NiGa$_2$O$_x$ with 90% CO–10% CO_2 when using the Ozawa–Flynn–Wall (OFW) method (details in the ESI†).

Comparison between the maximum CO_2 conversion of MGa$_2$O$_x$ (M = Ni, Cu, Co) and earlier reported In-based materials for RWGS-CL and the equilibrium conversion of conventional RWGS is presented in Fig. 1A, and the experimentally obtained data for MGa$_2$O$_x$ are presented, respectively, in the ESI† text and in Fig. S2–S5 (ESI†). Ga metal is known to have a very low melting point (302.8 K) on its own when reduced, but in this study Ga always remained in a composite (alloyed) state with other metals, and no melting or volatilization was observed before or after H_2 reduction. Actually, Cu–In$_2$O$_3$ and Co–In$_2$O$_3$ were both reported to show superior fast kinetics at medium temperatures. However, Cu–In$_2$O$_3$ showed no advantage for CO_2 conversion compared with the conventional RWGS.[25] Although Co–In$_2$O$_3$ displayed a maximum CO_2 conversion of 70–80% in the medium temperature region, which is higher than that of conventional RWGS, there is some room for improving it to conserve energy and decrease costs. Regarding MGa$_2$O$_x$ (M = Ni, Cu, Co), they showed a maximum CO_2 conversion of 99% at temperatures in the range of 673–973 K,
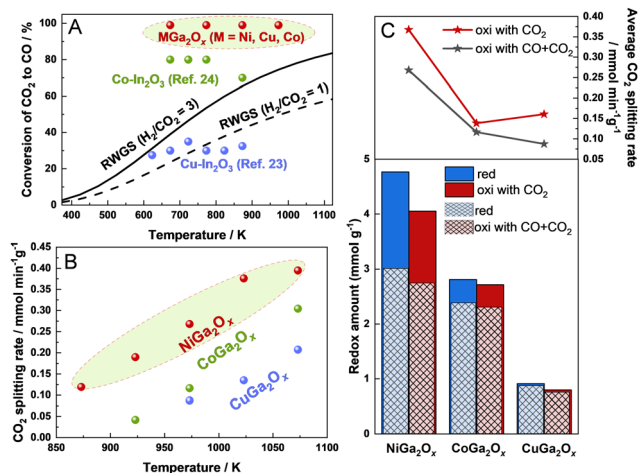

Fig. 1 (A) The maximum CO_2 conversion of Ga-based and In-based oxides for RWGS-CL and the equilibrium conversion of conventional RWGS. (B) The CO_2 splitting rates of MGa$_2$O$_x$ (M = Ni, Cu, Co) under a 90% concentration of CO. The data of CoGa$_2$O$_x$ were collected before reaching a stable state. (C) The redox amounts and average splitting rates of MGa$_2$O$_x$ (M = Ni, Cu, Co) at 973 K.

which is much higher than the equilibrium conversion of conventional RWGS and the materials reported earlier. This result indicates MGa$_2$O$_x$ (M = Ni, Cu, Co) as promising RWGS-CL materials with superior thermodynamical advantages.

The redox amounts and CO_2 splitting rates of NiGa$_2$O$_x$ and CuGa$_2$O$_x$ were all measured after sufficient H_2 pretreatment at 973 K until the following cycles became stable, but it is difficult for CoGa$_2$O$_x$ to reach a stable state, even when pretreated at a higher temperature for its low reduction rate, as confirmed by the combination of redox amounts and XRD (related descriptions are presented in Fig. S6 and S7, ESI†). Deeper pre-reduction at high temperatures will aggregate the particles and shrink the surface area (the results of BET are presented in Table S1, ESI†), consequently deteriorating the RWGS-CL performance. Therefore, we infer CoGa$_2$O$_x$ as an unsuitable material for RWGS-CL. However, the performance data of CoGa$_2$O$_x$ without reaching a stable state will still be presented as a comparison for the following discussion. The CO_2 splitting rates of MGa$_2$O$_x$ (M = Ni, Cu, Co) with 90% CO–10% CO_2 at different temperatures are shown in Fig. 1B. NiGa$_2$O$_x$ shows high average CO_2 splitting rates of 0.12, 0.19, 0.27, 0.38, and 0.39 mmol min^{-1} g^{-1} at 873, 923, 973, 1023, and 1073 K, respectively, even under a 90% concentration of CO, which is markedly higher than those of CoGa$_2$O$_x$ and CuGa$_2$O$_x$.

The CO_2 splitting rates and redox amounts of MGa$_2$O$_x$ (M = Ni, Cu, Co) at 973 K under different oxidation conditions (10% CO_2; 90% CO–10% CO_2) are presented in Fig. 1C. Generally, oxidation with CO + CO_2 decreases both the redox amounts and the CO_2 splitting rate compared with oxidation with only CO_2 because of the backward progress of the reverse reaction. Ni is a better dopant than Co and Cu in terms of the redox amount and CO_2 splitting rate under both CO_2 and CO + CO_2 oxidation conditions. The experimental results (Fig. S8 and ESI† text) indicate no by-product formation and negligible carbon

deposition using a fixed bed reactor equipped with a quadrupole mass spectrometer (Q-MS), which show the reliability and repeatability of our method. Moreover, comparisons of the CO_2 splitting rates and CO yields of the OSMs for RWGS-CL in the present work (with 10% CO_2) and in the literature are presented in Fig. S9 (ESI†). Actually, $NiGa_2O_x$ shows a relatively high CO_2 splitting rate and CO yield compared to those of the other reported OSMs.[8,11,13,16,19–21,26–28] In summary, $NiGa_2O_x$ showed high potential for RWGS-CL and was therefore selected for further study. The stability results of $NiGa_2O_x$ over 10 cycles at 973 K are shown in Fig. S10 (ESI†), exhibiting a slow decrease in the oxidation amounts and CO_2 splitting rates during cycling, which is partially attributable to the deep pre-reduction and repetitive cycles leading to partial shrinkage of the surface area of the material. The STEM-EDS results in Fig. S11 and BET results in Table S1 confirm the structure stability even after 10 cycles of reaction (details in the ESI†).

H_2-TPR measurements were conducted on different metal oxide samples for RWGS-CL analysis (Fig. 2A). Ga_2O_3 shows almost no reduction in the tested temperature range, the dopants of Ni, Co and Cu improve the reducibility of Ga_2O_3 to a different extent. $NiGa_2O_x$ exhibited a significantly higher H_2 consumption amount which started at a much lower temperature compared to $CoGa_2O_x$ or $CuGa_2O_x$, indicating the dopant of Ni outperforms Cu or Co in reducibility. Similarly, CO_2-TPO measurements (Fig. 2B) confirmed that the Ni dopant also outperforms Cu or Co in the oxidation ability. $NiGa_2O_x$ also shows a much higher surface area both after reduction and after oxidation than $CoGa_2O_x$ or $CuGa_2O_x$ according to the BET results (Table S1, ESI†). A larger surface area provides more reaction sites, allowing more reactant molecules to participate in the reaction simultaneously, leading to a better reaction rate for $NiGa_2O_x$. Moreover, the results of density functional theory (DFT) calculations show that the Ni-doping material displays a better CO adsorption ability than the other two, which is beneficial for Ni outperforming Cu and Co as a dopant (details in Fig. S12–S14 and Table S2 and ESI† text).

Structural and electronic properties were investigated using XRD, STEM-EDX, BET, and *in situ* XAFS. From the XRD spectra in Fig. 3A (left), the as-prepared sample shows only peaks of the $NiGa_2O_4$ spinel, manifesting the successful preparation of the target material. From the STEM-EDX images of the as-prepared $NiGa_2O_4$ (Fig. 3A (right), details in Fig. S15, ESI†), tens of
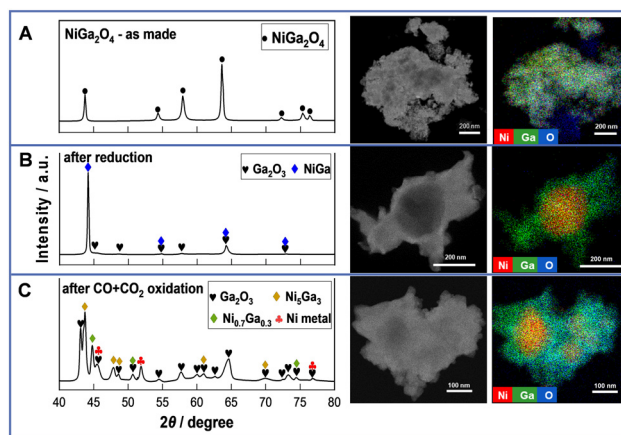

Fig. 3 XRD profiles (left) and STEM-EDX images (right) of $NiGa_2O_x$ (A) as-prepared, (B) after reduction and (C) after CO + CO_2 oxidation.

nanometers of polycrystalline particles are observed. The Ni and Ga species are all dispersed uniformly. Regarding the reduced $NiGa_2O_x$, the XRD profile exhibits peaks for the NiGa alloy and Ga_2O_3. Also, STEM-EDX images (Fig. 3B (right)) show aggregated Ni species during uniform dispersion of the Ga species. Moreover, the surface area is markedly reduced after the reduction because of the alloy formation. These findings manifest that all NiO and part of Ga_2O_3 are reduced to form the NiGa alloy, thus leaving part of the Ga_2O_3 unreduced. For the CO + CO_2 oxidized $NiGa_2O_x$, polycrystalline particles with a size of tens of nanometers are observed from STEM images, indicating that the particles will aggregate to larger ones after reduction and reoxidation by CO + CO_2 processing, thereby leading to a decreased surface area as shown in Table S1 (ESI†). Moreover, the XRD patterns display the peaks of Ga_2O_3, Ni metal and Ni–Ga alloy (Ni_5Ga_3 and $Ni_{0.7}Ga_{0.3}$). STEM-EDX images (Fig. 3C (right)) show consistent results of the partial aggregation of Ni species to form the Ni–Ga alloy during uniform dispersion of Ga species and the remaining part of Ni species. These illustrate that only part of the Ga species in the NiGa alloy are re-oxidized to Ga_2O_3 by CO + CO_2, whereas Ni species remain in a metallic state, acting as a part of the alloy or an individual element throughout the RWGS-CL process. Additionally, from the XRD results of the CO_2-only oxidized $NiGa_2O_x$ shown in Fig. S16 (ESI†), only Ni metal and Ga_2O_3 peaks were observed, with no peaks of the Ni–Ga alloy compared with the XRD results of CO + CO_2 oxidized $NiGa_2O_x$. This finding illustrates that the presence of CO influences the amount of the Ni–Ga alloy which can be re-oxidized in the oxidation step.

The *in situ* XAFS results of $NiGa_2O_x$ at 973 K are presented in Fig. 4. The XANES spectra on the Ga K-edge shift negatively to the spectrum of the pre-prepared half-reduced $NiGa_2O_4$ sample during the reduction and shift positively to the Ga_2O_3 spectrum during the CO + CO_2 reoxidation (Fig. 4A and B). These regular changes on the Ga K-edge during the RWGS-CL process provide evidence of the successful redox cycle of gallium. From the spectra of $NiGa_2O_x$ during CO_2 re-oxidation shown in Fig. S17A (ESI†), it is apparent that the spectra shift faster and finally
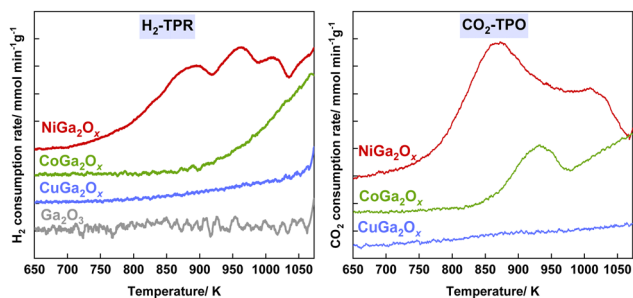

Fig. 2 (A) H_2-TPR and (B) CO_2-TPO of MGa_2O_x (M = Ni, Cu, Co).
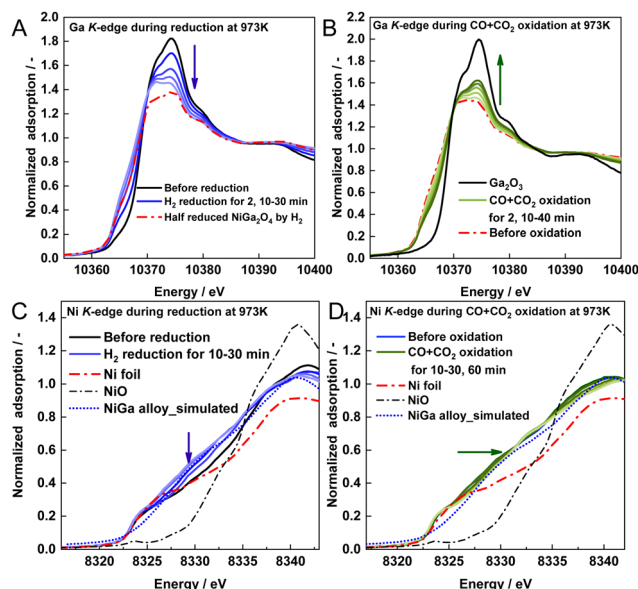
Fig. 4 XANES spectra of NiGa$_2$O$_x$ during (A) H$_2$ reduction and (B) CO + CO$_2$ oxidation on the Ga K-edge, and (C) H$_2$ reduction and (D) CO + CO$_2$ oxidation on the Ni K-edge.

become closer to that of Ga$_2$O$_3$ than that during CO + CO$_2$ reoxidation, indicating that the presence of CO in the oxidation step can be expected to restrain the progress of the oxidation of Ga.

From another perspective, Ni K-edge XANES spectra shift negatively toward the direction of the Ni spectrum with a slightly different peak shape during reduction (Fig. 4C) and very similar peak shapes to the simulated NiGa alloy spectrum obtained by calculation (calculation details in the ESI† text), thereby manifesting the formation of the NiGa alloy, except for Ni metal. During CO + CO$_2$ reoxidation, the spectra shift slowly to the Ni spectrum (Fig. 4D), manifesting that Ni metals are partially decomposed from the Ni–Ga alloy. Furthermore, the peak shapes are very different from those of NiO, indicating that no NiO was produced during the oxidation. Regarding the spectra of NiGa$_2$O$_x$ during CO$_2$ reoxidation in Fig. S17B (ESI†), the spectra shift faster and finally become closer to the Ni spectrum than those during CO + CO$_2$ reoxidation. This manifests that the presence of CO in the oxidation step can be expected to restrain the degree of decomposition of the Ni–Ga alloy.

Based on the analyses of structural and electronic properties, the proposed redox mechanism of NiGa$_2$O$_x$ during the RWGS-CL process in the presence of a high concentration of CO is shown in Fig. S18 (ESI†). Specifically, the Ni–Ga alloy is formed on Ga$_2$O$_3$ by H$_2$ reduction, with formation of oxygen vacancies. Then CO$_2$ is adsorbed and dissociated on the Ni–Ga alloy with progress of the oxidation step, thereby re-filling the oxygen vacancies. It is worth noting that the presence of CO in the oxidation step influences the NiGa$_2$O$_x$ performance by restraining the oxygen re-filling, leading to smaller amounts of Ga species for the key phase-change process.

In situ XAFS measurements were performed at the beamline BL14B2 of SPring-8 (Proposal No. 2022B1775). MEXT Project

Conflicts of interest

The authors have no conflicts of interest.

References

1 IPCC AR6: Climate Change 2021.
2 K. Tucki, O. Orynycz and M. Mitoraj-Wojtanek, *Energies*, 2020, **13**, 4127.
3 J. Artz, T. E. Müller, K. Thenert, J. Kleinekorte, R. Meys, A. Sternberg, A. Bardow and W. Leitner, *Chem. Rev.*, 2018, **118**, 434–504.
4 F. V. Vázquez, J. Koponen, V. Ruuskanen, C. Bajamundi, A. Kosonen, P. Simell, J. Ahola, C. Frilund, J. Elfving, M. Reinikainen, N. Heikkinen, J. Kauppinen and P. Piermartini, *J. CO$_2$ Util.*, 2018, **28**, 235–246.
5 C. Hepburn, E. Adlen, J. Beddington, E. A. Carter, S. Fuss, N. Mac Dowell, J. C. Minx, P. Smith and C. K. Williams, *Nature*, 2019, **575**, 87–97.
6 H.-H. Qiu and L.-G. Liu, *Energies*, 2018, **11**, 1103.
7 G. Centi, E. A. Quadrelli and S. Perathoner, *Energy Environ. Sci.*, 2013, **6**, 1711–1731.
8 D. Maiti, B. J. Hare, Y. A. Daza, A. E. Ramos, J. N. Kuhn and V. R. Bhethanabotla, *Energy Environ. Sci.*, 2018, **11**, 648–659.
9 M. Wenzel, L. Rihko-Struckmann and K. Sundmacher, *AIChE J.*, 2017, **63**, 15–22.
10 S. Y. Tee, K. Y. Win, W. S. Teo, L.-D. Koh, S. Liu, C. P. Teng and M.-Y. Han, *Adv. Sci.*, 2017, **4**, 1600337.
11 Y. A. Daza, D. Maiti, R. A. Kent, V. R. Bhethanabotla and J. N. Kuhn, *Catal. Today*, 2015, **258**, 691–698.
12 B. J. Hare, D. Maiti, S. Ramani, A. E. Ramos, V. R. Bhethanabotla and J. N. Kuhn, *Catal. Today*, 2019, **323**, 225–232.
13 A. E. Ramos, D. Maiti, Y. A. Daza, J. N. Kuhn and V. R. Bhethanabotla, *Catal. Today*, 2019, **338**, 52–59.
14 J. C. Brower, B. J. Hare, V. R. Bhethanabotla and J. N. Kuhn, *ChemCatChem*, 2020, **12**, 6317–6328.
15 Y. A. Daza, R. A. Kent, M. M. Yung and J. N. Kuhn, *Ind. Eng. Chem. Res.*, 2014, **53**, 5828–5837.
16 A. Jo, Y. Kim, H. S. Lim, M. Lee, D. Kang and J. W. Lee, *J. CO$_2$ Util.*, 2022, **56**, 101845.
17 H. Z. Shi, V. R. Bhethanabotla and J. N. Kuhn, *J. CO2 Util.*, 2021, **51**, 101638.
18 Y. A. Daza, D. Maiti, B. J. Hare, V. R. Bhethanabotla and J. N. Kuhn, *Surf. Sci.*, 2016, **648**, 92–99.
19 J. Rojas, E. Sun, G. Wan, J. Oh, R. Randall, V. Haribal, I.-H. Jung, R. Gupta and A. Majumdar, *ACS Sustainable Chem. Eng.*, 2022, **10**, 12252–12261.
20 L. Ma, Y. Qiu, M. Li, D. Cui, S. Zhang, D. Zeng and R. Xiao, *Ind. Eng. Chem. Res.*, 2020, **59**, 6924–6930.
21 Y. Qiu, L. Ma, D. Zeng, M. Li, D. Cui, Y. Lv, S. Zhang and R. Xiao, *J. Energy Chem.*, 2020, **46**, 123–132.
22 D. Zeng, Y. Qiu, L. Ma, M. Li, D. Cui, S. Zhang and R. Xiao, *Environ. Sci. Technol.*, 2020, **54**, 12467–12475.
23 J. I. Makiura, T. Higo, Y. Kurosawa, K. Murakami, S. Ogo, H. Tsuneki, Y. Hashimoto, Y. Sato and Y. Sekine, *Chem. Sci.*, 2020, **12**, 2108–2113.
24 J. I. Makiura, S. Kakihara, T. Higo, N. Ito, Y. Hirano and Y. Sekine, *Chem. Commun.*, 2022, **58**, 4837–4840.
25 X. Cui and S. K. Kær, *Ind. Eng. Chem. Res.*, 2019, **58**, 10559–10569.
26 F. J. Pomiro, G. G. Fouga, A. E. Bohé and G. De Micco, *J. Alloys Compd.*, 2023, **938**, 168671.
27 H. S. Lim, Y. Kim, D. Kang, M. Lee, A. Jo and J. W. Lee, *ACS Catal.*, 2021, **11**, 12220–12231.
28 H. Shi, V. R. Bhethanabotla and J. N. Kuhn, *J. Ind. Eng. Chem.*, 2023, **118**, 44–52.